Accepted Manuscript

Dual network extraction algorithm to investigate multiple transport processes in porous materials: Image-based modeling of pore and grain scale processes

Zohaib Atiq Khan , Tom Tranter , Mehrez Agnaou , Ali Elkamel , Jeff Gostick

Please cite this article as: Zohaib Atiq Khan , Tom Tranter , Mehrez Agnaou , Ali Elkamel , Jeff Gostick , Dual network extraction algorithm to investigate multiple transport processes in porous materials: Image-based modeling of pore and grain scale processes, *Computers and Chemical Engineering* (2018), doi: https://doi.org/10.1016/j.compchemeng.2018.12.025

Highlights

- SNOW DUAL algorithm framework to extract both solid and void phase pore network simultaneously.
- Algorithm includes connectivity and geometrical information of both void and solid phases as well as the interlinking of these phases with each other.
- Algorithm uses a novel and accurate means of calculating interfacial areas between grains and voids directly from digital images.
- Effective transport properties calculated from SNOW DUAL algorithm were found to agree well with numerical and experimental data.
- Resolution study showed good agreement for transport properties calculation.

Dual network extraction algorithm to investigate multiple transport processes in porous materials: Image-based modeling of pore and grain scale processes

Zohaib Atiq Khan[1,3], Tom Tranter[1], Mehrez Agnaou[1], Ali Elkamel[1,2], and Jeff Gostick[1,*]

[1] Department of Chemical Engineering, University of Waterloo, Waterloo, ON Canada

[2] Department of Chemical Engineering & GRC, Petroleum Institute, Abu Dhabi, UAE

[3] Department of Chemical Engineering, University of Engineering and Technology Lahore, Pakistan

[*] Corresponding Author: jgostick@uwaterloo.ca

Abstract

Image processing of 3D tomographic images to extract structural information of porous materials has become extremely important in porous media research with the commoditization of x-ray tomography equipment to the lab scale. Extracted pore networks from images using image analysis techniques enable transport properties calculation for bigger domains at a low computational cost, allowing pore-scale investigation of porous media over meaningful macroscopic length scales. The present study reports a pore network extraction algorithm to simultaneously extract void and solid networks from tomographic images of porous materials using simple image analysis techniques. Crucially, it includes connectivity and geometrical information of both void and solid phases as well as the interlinking of these phases with each other. Validation was obtained on networks extracted from simple cubic and random sphere packings over a range of porosities. The effective diffusivity in the void phase and thermal conductivity in the solid phase was then calculated and found to agree well with direct numerical simulation results on the images, as well as a range of experimental data. One important outcome of this work was a novel and accurate means of calculating interfacial areas between grains and voids directly from digital images, which is critical to many phenomena where phase interactions occur. The efficient 'dual network' algorithm is written in PYTHON using open source tools and provides a new way to study critical processes that depend on transport in both void and solid phase such as catalytic reactors and electrochemical systems.

Keywords

porous media, transport phenomena, heterogeneous catalysis, tomography, pore network modelling

1   Introduction

Transport in porous media plays an essential part in many prominent applications such as oil recovery and aquifer management in naturally occurring rocks and soils (Sahimi, 1993), but also devices containing engineered porous media such as battery electrodes (Aghighi and Gostick, 2017), filters (Zhang et al., 2017), membranes (Krishna, 2018) and catalyst particles (Sadeghi et al., 2017). Transport and reaction processes strongly depend on the void and solid structure. Two materials which have the same porosity can have drastically different transport and reaction rates because of differences in pore size, shape, and connectivity, etc (Liang et al., 2000). An often overlooked or neglected aspect of porous media studies is the transport in the solid phase (i.e. heat and electrons), which is subject to the same performance-structure competition as the void phase. In applications such as battery electrodes and catalysts supports, the solid structure provides reactive surface area and transport pathways. Moreover, the void and solid phases also impact the transport and reaction processes in opposing phases, so designing optimized materials with enhanced performance requires a detailed study of both phases simultaneously.

Visualization has always been a vital tool in porous media analysis, from optical imaging of serial sections and 2D micromodels, to modern tools such as FIB-SEM and X-ray tomography. High-resolution X-ray tomography has become the standard platform to understand the internal structure of porous media (Velev and Lenhoff, 2000). Most benchtop X-ray tomography scanners can produce 3D images of resolution as good as 1-μm voxel, while the recent generation can give a resolution of 20 nm (Schlüter et al., 2014a). The deluge of information provided by X-ray tomography (Sabharwal et al., 2016) has highlighted the need for efficient means of extracting valuable information from these tomograms given the massive size of the image, often over 1 billion elements (1000^3 voxels).

Quantitative image analysis can be used to obtain a range of information about void structure, such as the two-point correlation function (Ioannidis and Chatzis, 2000) or chord-length distribution (Torquato and Lu, 1993). However, finding the connectivity of void space from a porous material is one of the most important aspects since it is directly related to the most important properties: tortuosity and permeability. Researchers have tried to extract this structural information from tomographic images using many different algorithms. A network extraction algorithm that is widely used in pore network extraction is maximal ball algorithm by (Silin and Patzek, 2006), then adopted and developed by (Al-Kharusi and Blunt, 2007). Their method was time-consuming and tended to predict high coordination number. To prevent this issue, (Dong and Blunt, 2009) made a two-step algorithm that defines voids and throats

through a clustering process. In addition to these network extraction algorithms, (Lindquist et al., 1996) developed 3DMA software using medial axis transform. (Vogel and Roth, 2001) developed similar network extraction algorithms based on skeletonization techniques to characterize solid data. (Liang et al., 2000) performed void space partitioning based on morphological skeletonization by using fully parallel thinning algorithm. They investigated stochastically reconstructed porous media images and shows that identical porosities exhibit significance difference in geometry and connectivity. Pore network extraction using watershed segmentation was originally investigated by (Thompson et al., 2005) and (Sheppard et al., 2006).(Rabbani et al., 2014) used this approach to extract network for low porosity sandstone. (Agaesse et al., 2016) applied watershed segmentation on the gas diffusion layer of proton exchange membrane fuel cell. Recently, (Gostick, 2017) refined the watershed method for high porosity material by extracting a sub-network of the over-segmented watershed (SNOW). This algorithm succeeds by removing several types of spurious peaks in the distance transform that lead to over-segmentation in the watershed step, especially in high porosity images. Importantly, the SNOW algorithm was shown to generally work for both high and low porosity materials.

The commonality in these algorithms is that all of them have been tuned to find void phase structure since transport in the void is of general interest, while solid phase is often ignored. In many chemical engineering applications, however, electron and heat transport through the solid phase are equally important, which demands the need for solid structure extraction. In principle, any existing algorithm can be applied to the solid phase by inverting the image (Wildenschild and Sheppard, 2013), but this would only yield two independent networks, while the interactions and interconnections with void phase has significant importance. Heat can be transferred between the void and solid, and reactions happen at the void-solid interface. Consider a reaction-diffusion process in porous catalyst particles. Here solid phase requires consideration as the kinetics of chemical reaction is highly dependent on temperature, so modeling heat transfer within the particles is vital (Datta, 2007). Figure 1 shows a catalytic fixed bed reactor along with different transport phenomena taking place inside, including convective heat and mass transfer in void phase region, mass diffusion due to the concentration gradient between void and solid phase, reaction process occurring at the interface of catalyst particle and intraparticle heat conduction between catalyst particles. Therefore, in order to get maximum benefit from network modelling, it is necessary to extract a dual network that incorporates both void and solid phases as well as the local interconnection of these phases with each other.

In this work, we present an algorithm that simultaneously extracts both the solid and void network from a tomographic image, including the interlinking of these phases with each other, to create a 'dual network'. The presented algorithm is an extension of the recently published SNOW algorithm (Gostick, 2017),

which was selected based on its low computational cost, applicability to high porosity materials, and ability to reliably extract the key structural features. The presented algorithm provides a new avenue for pore network modelling, opening the way to investigate many critical processes that require transport in both void and solid phase such as reaction-diffusion in catalyst particles and charging and discharging dynamics of porous electrodes in batteries. To the best of our knowledge, this is first dual network extraction effort in pore network modelling.

2   Algorithm

The watershed segmentation algorithm has many benefits for network extraction, but most appealingly it matches the intuitive definition of what constitutes a pore body, as discussed by (Blunt, 2017) in his recent monograph. In the present study the watershed approach was used, building on the recently published report of the SNOW extraction algorithm (Sub-Network of an Over-segmented Watershed) (Gostick, 2017). The general procedure to extract only void network is outlined in Figure 2a. The algorithm works in two steps. This first is the partitioning of the image into discrete regions for each pore, and the second is to analyze the regions in the partitioned image to extract geometrical and topological information for the network. The procedure starts with a binary image of 0's as solid phase and 1's as void phase, then performs distance transform on it the void. A maximum filter is applied to find peaks which will become the basins of the watershed transform, but first any extraneous peaks are trimmed which is the key to avoiding over-segmentation. In the next step, marker-based watershed segmentation is performed on the remaining peaks to get void regions as catchment basins in the network. Lastly, the segmented image is scanned one region at a time to extract the network information such as pore size and neighbors. The details of all relevant geometrical properties can be found in our prevoius work (Gostick, 2017).

2.1   Detailed Description of Dual Network Extraction Algorithm

The dual network extraction algorithm presented here was developed on the premise that the analysis of the partitioned image is agnostic to the whether the regions are void, solid or either. As such, the basic outline of the algorithm is that the void and solid phases are partitioned using the normal approach described above, but the two images are combined into a single composite image prior to extracting the geometrical and topological information for each region. A post processing step determines which regions belong to each phase and labels them accordingly. The present incarnation of the algorithm also includes the ability to include boundary nodes on the image prior to extraction, so they appear in the resultant network. The basic framework of the dual network is shown in Figure 2b and discussed in following sections. The open source code is implemented in PYTHON using the SCIPY stack (Jones et al., 2001) and is provided as part of PoreSpy (Gostick, 2018).

2.1.1 Applying SNOW algorithm

Given a binary image with 1's indicating void and 0's for solid, the SNOW algorithm is applied to both void and solid phase separately giving the result shown in Figure 3. While applying SNOW on the solid phase, the image was inverted to represent solid by 1's and void by 0's. The SCIKIT-IMAGE package was used to apply marker-based watershed segmentation (van der Walt et al., 2014).

2.1.2 Merging watershed segmentations

Next the void and solid phase segmentations are merged into a single composite image. The largest value of peak label in the void segmentation was added to solid phase segmentation in order to differentiate between void and solid properties labels (thus void regions are labelled $1 \rightarrow N_V$, and solid regions $N_V + 1 \rightarrow N_V + N_S = N_T$). Figure 3(a,b) represents watershed segmentation applied on void and solid phase independently. In Figure 3c the merged watershed segmentation of void and solid phases is shown with void labelled as 1,2,3,4 and 5 and solid labelled as 6,7, and 8. Similarly, the distance transforms of void and solid phase were also merged in order to provide combined distance transform; this is necessary so the sizes of the underlying region, such as diameter of an inscribed sphere, can be found during the network extraction phase.

2.1.3 Defining boundary nodes

Defining boundary conditions in an irregular pore network is a challenging task because of rough surfaces at boundary faces. This problem gets more complicated in the dual network as now two phases with different voids and solid orientation exist at the boundary of the network. These irregular faces lead to many difficulties during simulation of transport process. Firstly, domain length and area cannot be calculated precisely, which can either over- or underestimate the effective property calculation (e.g. effective diffusivity) which depend on domain area and length. It is also difficult to calculate flux as there is no definitive control surface which complicates simulation of transport process. This issue was discussed in previous work (Gostick, 2013) for randomly generated Voronoi and Delaunay network. In that work a method ws developed to create flat boundary faces by mirroring the base points outside the working domain and trimming outside pores after tessellation. A similar approach was applied in the present work:

The merged watershed segmentation containing both phases was padded with a layer of extra voxels. This process copied the void and solid labels at the surface of the image and formed an external layer of void and solid labels. Subsequently, all labels on the padded surface were given new values (starting at $N_T + 1$ where N_T was the total number of labels in the merged watershed image) so that they could be extracted as separate nodes in the dual network. In the next step, interconnections of boundary nodes with each other were prevented by using the SCIPY-NDIMAGE *find_boundaries* function. This created a boolean

mask of boundary faces identifying boundary nodes interconnections location which was then labelled as 0's to represent a border region between bounadry labels. Note that any values in the watershed image labelled 0 will be ignored during the network extraction step. Figure 4 shows segmented images with and without specifying boundary nodes. The black colour on the boundary surfaces represents fictitious solid regions to avoid interconnections of boundary nodes, while coloured regions show boundary nodes interconnected with adjacent void/solid inside the segmented image.

2.1.4   Extracting Dual Network Information

After defining boundary nodes, the merged watershed segmentation and distance transform were scanned to extract the geometrical and topological properties of the void, solid and throats. The process treats all labelled segments as voids (or more generally nodes) so calculates the connectivity and geometrical properties of the solid phase by treating it as a void phase. To measure size, area, volume etc. each labelled region is isolated from its neighbouring region and the number of voxels associated with the specific geometrical property are analyzed. Similarly, throat properties are calculated by scanning neighbouring regions and analyzing the size of the boundary defined by shared voxels. This process is outlined in detail in previous work (Gostick, 2017).

2.1.5   Labeling Phases and Finding Interconnections

The output of the previous step contains no information about which nodes or connections belong to which phase, so a post-processing procedure was necessary. The data from the previous step was stored in arrays of length N_T or N_C, where N_T is the total number of nodes in the network (solid + void) and N_C is the total number of connections. Because of the way the regions were numbered it is known that the first N_V entries correspond to voids and the remaining N_S values the solid phase. Similarly, the connections can be identified by the node numbers being connected. The options are void-to-void, solid-to-solid, and void-to-solid. All this information is stored by labeling each entry accordingly.

2.1.6   Finding interface surface area

The interfacial area between two nodes is one of the most critical aspects of the geometric analysis, but it is difficult to determine. Two neighboring regions share a common set of voxels, so analyzing the shape of this common set can provide a wealth of information about the connection between the regions, such as interfacial surface area. For instance, as shown in Figure 3c void 1 is connected with grains 6 and 7, and grain 8 shares surface area with voids labelled as 3,4 and 5. Although simple in principle, surface areas are difficult to determine in a voxel image (Culligan et al., 2004). In the present work this was accomplished using the marching-cubes algorithm (Lewiner et al., 2003) but a few considerations were necessary. The marching-cubes algorithm operates by constructing a tetrahedral mesh around the perimeter of the region, and the surface area can be found from the triangular facets on the exterior

surface. The quality of the mesh is dependent on the input image however. For instance, a Boolean image will result in a mesh that conforms exactly to the voxel facets so the area estimate will be no better than just counting cube faces. An image with blurry boundaries allows the algorithm to construct a smoother mesh, so in the present work each region was subjected to mean filter with a 3^3 cubic structuring element prior to analysis. It was confirmed on images of single spheres at different resolutions that this approach yields the correct value within 5% as long as diameter of voids or solids is more than 10 voxels. The other consideration is that the marching cubes algorithm does not work well on 2D (or nearly 2D) regions, so the interface between two regions cannot be analyzed directly. A simple and elegant workaround was developed here, whereby the surface area of region A and region B were found independently, and then for A and B combined. The interfacial surface area between A and B can be found from the sum of the individual areas, minus the combined area, then halved.

2.2 Generation of Sphere Packings for Validation

For validation of the extracted networks, images of simple cubic and random sphere packings of monosized spheres were used. These were generated using open source discrete element software Yade (Šmilauer and Chareyre, 2015). For simple cubic packing *regularOrtho* function was used to get 45 equal sized spheres of 50 voxels diameter ($\varnothing$) in a rectangular chamber of $148 \times 148 \times 249$ voxels size in x, y and z coordinates respectively. As shown in Figure 5a. This packing was used for direct validation discussed in detail in algorithm validation section. The *SpherePack* function was used to generate random spheres packing in a 525^3 voxels container. After generation, periodic compression was performed with *PerilsoCompressor* to stuff as many spheres as possible. The final porosity of random sphere packing after compression was 0.44.

It was of interest to validate the extracted networks on packings of various porosities, but sphere packings always have a porosity near 0.44, so instead the spheres were dilated to create overlaps. This overlapping was analogous to a sintering effect in solid phase which gradually decreased the porosity (ε) from 0.44 to 0.052 (Bertei et al., 2013). 2D slices of four different porosities packings are shown in Figure 6. It can be seen clearly that some spheres at low porosity overlap into each other and form a cluster of solid phase while many voids are isolated from neighbouring voids in void phase. Overall eight different porosity packings were used to investigate the performance of the dual network across a range of scenarios.

3 Results and Validation

3.1 Validation on Periodic Packings

3.1.1 Topology and Geometry Structure

The present algorithm was validated directly by comparing the extracted network to that of simple packing which have known coordination number and size distribution in both void and solid phase. For this purpose, regular orthogonal cubic packing of porosity 0.487 and sphere diameter of 50 voxels was chosen, as shown in Figure 5a. It has a nominal coordination number of 6 (surface, edge and corner sites have less) and known solid radius of 25 voxels. The total size of the container in x, y and z coordinates was $148 \times 148 \times 249$ voxels respectively. After applying the present algorithm, the resulting extracted network can be seen in Figure 5b. The solid, voids and throats of individual phases are shown in copper and silver colour respectively. Similarly, interconnections between solid and void phase, as well as, boundary throats are shown in green and red colour respectively. For better visualization, a representative unit cell of cubic packing is shown in Figure 5c. Each solid is connected with 6 neighbouring spheres and 8 neighbouring voids with a total coordination number of 14. The diameter of solids and their respective throats in the extracted network is approximately 50 voxels and 7 voxels. For void phase, the coordination number depends on the location of a void in the image. Each void is connected with 6 neighbouring voids, as well as interconnected with solid spheres depending upon its location (surface, edge, or corner). The total coordination number in void phase is 7, 8, 10 and 14 at corners, edges, faces and inside body respectively. Unlike solid phase, the size of voids and throats depends on their location in the extracted network. The diameter is highest inside body of cubic packing while it is lowest at edges and corners, which occurs because the walls of the container are implicitly included in the extraction. Table 1 shows a comparison of extracted and theoretical values of the packing obtained by summing up voxels of the image for a particular property. These results show a very good match of the structural properties in both void and solid phase of simple cubic packing.

3.1.2 Interfacial Surface Area

Validation of interfacial surface area of individual solid and void for irregular geometries is a challenging task because there is no analytical solution to compare against given the random nature of the particle contacts. In the present study, validation is performed on a regular cubic packing, which allows the exact determination of interfacial area of solid and void from analytical expressions. Figure 7 shows the structure of a single void connected with solid grains in a regular cubic packing. The area associated with neighbouring solids and voids are represented as green and yellow colored faces respectively. The total surface area of the void structure and solid grain calculated analytically are given in

Table *2*. The surface area of the void structure was calculated analytically according to:

$$A_s = 24r^2 - 2\pi r^2 - 6\pi r_{st}^2 - 24r_{st}.w \tag{1}$$

where r is the radius of spherical grain, r_{st} is the radius of the throat between two spherical grains and w is the width of the corner in the void structure. The value of $r_{st} = 6$ and $w = 2$ voxels were obtained by visual examination of the 3D image.

Equation 2 was then used to find the surface area A_c of region 1 associated with region 2. The intraphase and interphase parts are determined by checking if the two connecting regions belong to same or different phase respectively

$$A_c = \frac{1}{2}(A_{region\ 1} + A_{region\ 2} - A_{combined}) \tag{2}$$

where $A_{region\ 1}$ and $A_{region\ 2}$ is the surface area of region 1 and region 2 respectively while A_c is the surface area of region 1 associated with region 2 as shown in Figure 7c.

Also shown in

Table *2* are the interfacial surface areas between the void and solid as determined using the image analysis technique outlined in Section 2.1.6. There is less than 5% error between these two values, indicating a good agreement between SNOW DUAL estimated area and analytical solution.

3.2 Validation on Random Packings: Transport Properties

Although direct validation on a well-defined periodic packing gives insight into the accuracy of the extracted dual network, more realistic packings are of interest. A validation study was carried out by simulating the effective thermal and diffusive conductivity in the solid and void phase respectively of a random packing of spheres and comparing the results with other modelling methods and published experimental data where available. A dual network was extracted from a 525^3 voxel image containing 1250 spheres as shown in Figure 8. The initial diameter of all spheres was 50 voxels, but they were morphologically opened using a 1 voxel spherical structuring element to ensure they fully touched each other and avoid digitization artifacts. The void and solid phases are shown in silver and copper while interconnections and boundary throats are coloured green and red respectively.

In order to estimate steady-state thermal conductivity in the solid phase network, heat flow into and out of each solid sphere was calculated. For each sphere, i, in the solid phase network, thermal equilibrium requires that:

$$\sum_{i=1}^{n} J_i = 0 \tag{3}$$

where J is heat flow in W and n is the number of contacts of the sphere *i.e* number of thermal conductance elements connected with sphere i under consideration. In this simulation, steady-state Fourier's law was applied to calculate heat flow in the solid phase. Heat conduction between sphere i at temperature T_i and sphere j at temperature T_j can be calculated according to the following discretized form of the 1-dimensional Fourier equation:

$$j_{i,j} = kA\frac{(T_i - T_j)}{\Delta x} = g_{i,j}(T_i - T_j) \tag{4}$$

where k is bulk thermal conductivity of the material in *W/m.K*. A is the area of cross-section in m^2 between sphere i and j and x *(m)* is the length between sphere i centroid to sphere j centroid. These terms can be represented as thermal conductance $g_{i,j}$. Moreover, since the area between sphere i and j is not uniform, the term $g_{i,j}$ with an interconnected throat k is calculated using linear resistor theory for resistors in series:

$$\frac{1}{g_{i,j}} = \frac{1}{g_{i,k}} + \frac{1}{g_k} + \frac{1}{g_{k,j}} \tag{5}$$

For the thermal conductance calculation, the connections between spheres resulted in a situation where g_k in equation 5 was 0 since the length of the neck between the two grains was 0. Even as the grains where dilated to decrease the porosity, and new connections where made, the neck (or throat) had 0 length. This is illustrated in Figure 9a.

The thermal conductance in each sphere was determined by accounting for the nonuniform area of the sphere cross-section by representing the sphere with an equal volume pyramid as shown in Figure 9a. Although an exact geometrical model could be obtained for the spherical cross-section of the grains, this was not possible for the void space as discussed below, so the same pyramidal approximation was applied to both phases. The resulting expression for solid phase thermal conductance in sphere i can be calculated by the following expression:

$$g_{i,k} = 4k \frac{r_i r_k}{\Delta x_i} \tag{6}$$

where r_i and r_k are radii of sphere i and constriction, respectively, while Δx_i is the length of sphere i from the centroid to constriction boundary.

An analogous approach was adopted to estimate steady-state effective diffusivity in the void phase. Therefore, 1-D Fick's laws for steady state and diffusive conductance between void i and j can be represented in discretized form as equation 7, 8 and 9 respectively.

$$\sum_{i=1}^{n} q_i = 0 \tag{7}$$

$$\dot{q}_{i,j} = \frac{DA}{RT} \frac{(p_i - p_j)}{\Delta x} = d_{i,j}(p_i - p_j) \tag{8}$$

$$\frac{1}{d_{i,j}} = \frac{1}{d_{i,k}} + \frac{1}{d_k} + \frac{1}{d_{k,j}} \tag{9}$$

where q is the molar flow rate in *mol/s*. p is the partial pressure of the gas in the respective void. D is bulk diffusion coefficient of specie in void phase, d is diffusive conductance in void phase, T is the temperature of voids and R is universal gas constant.

Unlike the solid phase, the pores in the void phases did not form overlapping spheres, but instead consisted of inscribed spheres at the interstices of the grains, and throats connecting them. This is shown in Figure 9b. The same pyramidal shape was applied to the void pores as for the solid grains, resulting in the following formula:

$$d_{i,k} = \frac{4D}{RT} \frac{r_i r_k}{\Delta x_i} \tag{10}$$

The total conductance between pores also included a throat section. The value of d_k in equation 7 was found by assuming the throat has a square cross-sectional area that did not vary, thus:

$$d_k = \frac{4D}{RT} \frac{r_k^2}{L} \qquad (11)$$

where L is the length of the throat.

Boundary conditions in both solid and void phase were applied to opposite faces of the extracted network in the x-direction. The temperature of the solid at x = 0 and x = 525 μm was set to 373K and 298 K respectively. The spherical particle was assumed to be of copper material with intrinsic thermal conductivity k of 385 $W/m.K$. Similarly, the partial pressure oxygen in void phase at $x = 0$ and $x = 525$ μm was fixed to 21 kPa and 0 kPa respectively and oxygen bulk diffusivity D of 2.09×10^{-5} m^2/s in air was assumed in void phase.

The simulation performed in solid and void phase on the extracted dual network using OpenPNM (Gostick et al., 2016) open-source software, yielding the temperature and concentration profiles shown in Figure 10. Moreover, algorithm validation was performed by comparing the results of effective transport properties with lattice Boltzmann and random walker simulation (Chandrasekhar, 1943), which are described in more detail in the following sections.

3.2.1 Lattice-Boltzmann Simulation

Lattice-Boltzmann calculations were performed using the open-source software Palabos to model steady state conduction and diffusion in solid and void phase. D3Q7 lattice was used as descriptor and Bhatnagar–Gross–Krook (BGK) collision model was used to describe dynamics of heat and mass flow. A tolerance value of 10^{-4} was selected to calculate normalized values of effective transport properties. The simulation was carried out along all three axes of 525^3 mm^3 image and an average value of the effective property is reported. The main benefit of the LBM solver is that the voxel image is used directly as the computational mesh, thereby avoid the time consuming and error prone process of creating a mesh suitable for FEM solvers.

3.2.2 Random Walker Simulation

Discrete-time random walker method was used to find the tortuosity of solid and void phase in random sphere packing by calculating the mean square displacement of 1×10^5 random walkers. The method and its open-source, parallelized implementation are described in detail in a recent work (Tranter et al., 2018) The probability density function p(x,t) of a walker at location x and time t (Codling et al., 2008) can be described according to the equation 12:

$$p(x,t) = \frac{1}{\sqrt{4\pi Dt}} \exp\left(\frac{-x^2}{4Dt}\right) \tag{12}$$

The variance of equation 9 is termed as mean square displacement (MSD) and can be written as:

$$MSD = \int_{-\infty}^{\infty} x^2 p(x,t) dx \tag{13}$$

The mean square displacement (MSD) of a simple walker with unbiased movement is assumed to follow a Gaussian distribution and the gradient of MSD when plotted over a period of time gives tortusity factor $\tau\tau^{-1}$. The tortuosity $\tau\tau$ calculated is used to find effective coefficient in sphere packing of known void fraction ε according to (Davies, 1984):

$$\frac{D_{eff}}{D} = \frac{\varepsilon}{\tau} \tag{14}$$

The normalized effective conductivity as a function of solid fraction for SNOW DUAL, lattice Boltzmann and random walker simulation is shown in Figure 11a. The results of Koh, 1971 reported by (Agapiou and DeVries, 1989) for 304L stainless steel spherical powder is also shown. From the graph, it can be seen that SNOW dual results agree well with other modelling approaches for spherical particles. The normalized value of effective conductivity increases with increasing solid fraction. This agrees with equation 4 as at high solid fraction more area is exposed for heat conduction in the solid phase. Moreover, as tortuosity factor in equation 14 decreases with increasing solid fraction, effective conductivity value becomes higher at high solid fraction. Figure 11b shows the normalized effective diffusivity value against void fraction in spherical particles. The results obtained by (Bertei et al., 2013) and (Currie, 1960) are also reported, which agree well with SNOW Dual simulation. The effective diffusivity values decrease with increasing sintering effect in the solid phase. At 0.045 solid volume fraction almost no diffusion takes place in void phase because of high tortuosity and small exposed area available for diffusion.

3.3   Resolution Study

In order to check the robustness of dual extraction, a resolution study was conducted. Random sphere packings were produced as described above and spheres of diameter 54 voxels were inserted into the image containing 525^3 voxels. The resolution of the image was changed by decreasing or increasing the number of voxels using nearest neighbor interpolation. The resulting values of effective conductivity and effective diffusivity in solid and void phase as the resolution was varied from 0.5 to 1.7 of the original image is shown in Figure 12. At low resolution, the relative error in both void and solid phase at resolution 0.5 was 3.8% and 16% respectively which is acceptable to get preliminary results with low computational cost and low memory (RAM) usage while simulating bigger porous material domains which is currently not feasible in direct numerical simulation and lattice-Boltzmann modelling. It should

be noted that robust behavior towards resolution is not expected to translate to images noisey images. Obtaining clean and correct segementations from greyscale images remains a challenge (Schlüter et al., 2014b).

3.4 Performance

Modern X-ray tomography scanners can produce images at a high resolution of 1000^3 voxels or more, so any network extraction algorithm must process this large amount of data in a realistic time. Moreover, the algorithm should run on easily accessible computational resources such as desktop computers or laptops rather than depending on supercomputers. Good computational performance was ensured while developing dual network extraction algorithm by using Numpy array operations and the scipy.ndimage library for image analysis. Figure 13 shows algorithm run time as a function of image size. Five image sizes, from 200^3 to 1000^3 voxels, were used to analyze performance. The total function time includes the time required to apply SNOW algorithm on both pore and solid phase, as well as processing time of SNOW_DUAL. For 600^3 voxels image, it takes 37 minutes to extract whole dual network, which is passable though speed-ups would be welcome.

Although the dual network extraction algorithm is light in terms of computational resources, the watershed segmentation step in SNOW algorithm requires large RAM for images with billions of voxels. Figure 13 shows the amount of RAM usage in SNOW algorithm for different image sizes. It can be seen that until 400^3 voxels image size, the RAM usage is below 16 GB, indicating easy implementation of code on a normal workstation. An image having a size of 1000^3 voxels requires approximately 50 GB RAM and network extraction time is close to 3 hours. This huge amount of RAM usage can be avoided by using a low-resolution image which is discussed in the Resolution Study section above. The watershed step is also computationally slow, comprising the majority of the extraction time. A recent article by (Kornilov and Safonov, 2018) compares performance of different watershed implementations, although preliminary testing suggests that the difference disappear when images approach 1000^3 and have hundreds of basins.

The computational performance of extracted dual network was also compared with random walker simulation and lattice boltzmann simulation. The CPU processing time and RAM usage for all 8 samples in random sphere packings were measaured on both solid and void phases to find effective thermal conductivity and diffusivity repectivley. The computational study was performed on a Dell prescison T5500 workstation with Xeon X5650 processor (12 Cores) and 72 GB of RAM. For the LBM and RW simulations 10 cores were used, while for the PNM simulations all Python UMFPACK module was used which utilizes all 12 cores of CPU. The results are shown in Figure 14. It can seen the the dual network is

relatively more efficient in comparision with random walker and lattice boltzmann simulation. **Error! Reference source not found.**

4   Conclusions

The motivation behind the current study was to investigate the transport processes in porous materials at the microstructural level. The transport of reactive species in the void phase and heat and/or electrons in the solid phase is of central interest to chemical engineers wishing to design or analyze porous catalyst structures, but traditional porous media research almost exclusively neglects transport in the solid phase. The advent of x-ray tomographic imaging can provide extremely detailed images of the internal structures, but computer modeling remains prohibitively expensive. The present work utilized an alternative approach to modeling transport at the pore-scale by extracting network models from the images, thereby achieving an extremely significant model-order reduction. The novelty of the present approach is that both void and solid phase networks are extracted simultaneously, including the interconnections between the phases. Additionally, an elegant and accurate scheme for determining the interfacial surface area was developed, which is not straightforward for voxelized images.

The model output was validated directly on simple cubic packing with known connectivity and void/solid sizes, and the network properties were in good agreement with the known structural information of simple cubic packing. Simulation were also performed on random sphere packing by calculating effective conductivity and diffusivity in solid and void phase respectively. The results were compared with LBM, random walker and experimental data and were found in good agreement across a wide range of porosities. The current work opens a new avenue to study void-solid interations in reactive systems where microstructural features such as connectivity, interfacial contact, and heterogeneity play a significant role in performance.

5   Acknowledgements

6 References

Agaesse, T., Lamibrac, A., Büchi, F.N., Pauchet, J., Prat, M., 2016. Validation of pore network simulations of ex-situ water distributions in a gas diffusion layer of proton exchange membrane fuel cells with X-ray tomographic images. J. Power Sources 331, 462–474. https://doi.org/10.1016/j.jpowsour.2016.09.076

Agapiou, J.S., DeVries, M.F., 1989. An Experimental Determination of the Thermal Conductivity of a 304L Stainless Steel Powder Metallurgy Material. J. Heat Transfer 111, 281–286. https://doi.org/10.1115/1.3250675

Aghighi, M., Gostick, J., 2017. Pore network modeling of phase change in PEM fuel cell fibrous cathode. J. Appl. Electrochem. 47, 1323–1338. https://doi.org/10.1007/s10800-017-1126-6

Al-Kharusi, A.S., Blunt, M.J., 2007. Network extraction from sandstone and carbonate pore space images. J. Pet. Sci. Eng. 56, 219–231.

Bertei, A., Nucci, B., Nicolella, C., 2013. Effective transport properties in random packings of spheres and agglomerates. Chem. Eng. Trans. 32, 1531–1536. https://doi.org/10.33032/CET1332256

Blunt, M.J., 2017. Multiphase Flow in Permeable Media: A Pore-Scale Perspective. Cambridge University Press, Cambridge. https://doi.org/DOI: 10.1017/9781316145098

Chandrasekhar, S., 1943. Stochastic Problems in Physics and Astronomy. Rev. Mod. Phys. 15, 1–89. https://doi.org/10.1103/RevModPhys.15.1

Codling, E.A., Plank, M.J., Benhamou, S., 2008. Random walk models in biology. J. R. Soc. Interface 5, 813–834. https://doi.org/10.1098/rsif.2008.0014

Culligan, K.A., Wildenschild, D., Christensen, B.S.B., Gray, W.G., Rivers, M.L., Tompson, A.F.B., 2004. Interfacial area measurements for unsaturated flow through a porous medium. Water Resour. Res. 40, 1–12. https://doi.org/10.1029/2004WR003278

Currie, J.A., 1960. Gaseous diffusion in porous media. Part 2. - Dry granular materials. Br. J. Appl. Phys. 11, 318.

Datta, A.K., 2007. Porous media approaches to studying simultaneous heat and mass transfer in food processes. I: Problem formulations. J. Food Eng. 80, 80–95. https://doi.org/10.1016/j.jfoodeng.2006.05.013

Davies, C.N., 1984. Gas transport in porous media: The dusty-gas model. J. Aerosol Sci. 15, 81.

https://doi.org/10.1016/0021-8502(84)90058-2

Dong, H., Blunt, M.J., 2009. Pore-network extraction from micro-computerized-tomography images. Phys. Rev. E. Stat. Nonlin. Soft Matter Phys. 80, 36307. https://doi.org/10.1103/PhysRevE.80.036307

Gostick, J.., 2018. PoreSpy: A set of tools for characterizing and analying 3D images of porous materials. https://github.com/PMEAL/porespy.

Gostick, J., Aghighi, M., Hinebaugh, J., Tranter, T., Hoeh, M.A., Day, H., Spellacy, B., Sharqawy, M.H., Bazylak, A., Burns, A., Lehnert, W., Putz, A., 2016. OpenPNM: A Pore Network Modeling Package. Comput. Sci. Eng. 18, 60–74. https://doi.org/10.1109/MCSE.2016.49

Gostick, J.T., 2017. Versatile and efficient pore network extraction method usingmarker-based watershed segmentation. 1 Phys. Rev. E 003300, 1–11. https://doi.org/10.1103/PhysRevE.00.003300

Gostick, J.T., 2013. Random Pore Network Modeling of Fibrous PEMFC Gas Diffusion Media Using Voronoi and Delaunay Tessellations. J. Electrochem. Soc. 160, F731–F743. https://doi.org/10.1149/2.009308jes

Ioannidis, M.A., Chatzis, I., 2000. On the geometry and topology of 3D stochastic porous media. J. Colloid Interface Sci. 229, 323–334. https://doi.org/10.1006/jcis.2000.7055

Jones, E., Oliphant, T., Peterson, P., Others, 2001. SciPy: Open source scientific tools for Python: available at https://www.scipy.org/.

Kornilov, A., Safonov, I., 2018. An Overview of Watershed Algorithm Implementations in Open Source Libraries. J. Imaging 4, 123. https://doi.org/10.3390/jimaging4100123

Krishna, R., 2018. Methodologies for screening and selection of crystalline microporous materials in mixture separations. Sep. Purif. Technol. https://doi.org/10.1016/j.seppur.2017.11.056

Lewiner, T., Lopes, H., Vieira, A.W., Tavares, G., 2003. Efficient Implementation of Marching Cubes' Cases with Topological Guarantees. J. Graph. Tools 8, 1–15. https://doi.org/10.1080/10867651.2003.10487582

Liang, Ioannidis, Chatzis, I., 2000. Geometric and Topological Analysis of Three-Dimensional Porous Media: Pore Space Partitioning Based on Morphological Skeletonization. J. Colloid Interface Sci. 221, 13–24. https://doi.org/10.1006/jcis.1999.6559

Lindquist, W.B., Lee, S.-M., Coker, D.A., Jones, K.W., Spanne, P., 1996. Medial axis analysis of void

structure in three-dimensional tomographic images of porous media. J. Geophys. Res. Solid Earth 101, 8297–8310. https://doi.org/10.1029/95JB03039

Rabbani, A., Jamshidi, S., Salehi, S., 2014. Journal of Petroleum Science and Engineering An automated simple algorithm for realistic pore network extraction from micro-tomography images. J. Pet. Sci. Eng. 123, 164–171. https://doi.org/10.1016/j.petrol.2014.08.020

Sabharwal, M., Pant, L.M., Putz, A., Susac, D., Jankovic, J., Secanell, M., 2016. Analysis of Catalyst Layer Microstructures: From Imaging to Performance. Fuel Cells 16, 734–753. https://doi.org/10.1002/fuce.201600008

Sadeghi, M.A., Aghighi, M., Barralet, J., Gostick, J.T., 2017. Pore network modeling of reaction-diffusion in hierarchical porous particles: The effects of microstructure. Chem. Eng. J. 330, 1002–1011. https://doi.org/10.1016/j.cej.2017.07.139

Sahimi, M., 1993. Flow phenomena in rocks: from continuum models to fractals, percolation, cellular automata, and simulated annealing. Rev. Mod. Phys. 65, 1393–1534. https://doi.org/10.1103/RevModPhys.65.1393

Schlüter, S., Sheppard, A., Brown, K., Wildenschild, D., 2014a. Image processing of multiphase images obtained via X-ray microtomography: A review. Water Resour. Res. 50, 3615–3639. https://doi.org/10.1002/2014WR015256

Schlüter, S., Sheppard, A., Brown, K., Wildenschild, D., 2014b. Image processing of multiphase images obtained via X-ray microtomography: A review. Water Resour. Res. 50, 3615–3639. https://doi.org/10.1002/2014WR015256

Sheppard, A.P., Sok, R.M., Averdunk, H., Robins, V.B., Ghous, A., 2006. Analysis of Rock Microstructure Using High- Resolution X-Ray Tomography. Proc. Int. Symp. Soc. Core Anal. 1–12.

Silin, D., Patzek, T., 2006. Pore space morphology analysis using maximal inscribed spheres. Phys. A Stat. Mech. its Appl. 371, 336–360. https://doi.org/10.1016/j.physa.2006.04.048

Šmilauer, V., Chareyre, B., 2015. DEM formulation, in: Yade Documentation 2nd Ed. The {Y}ade Project. https://doi.org/10.5281/zenodo.34044

Thompson, K.E., Willson, C.S., White, C.D., Nyman, S., Bhattacharya, J., Reed, A.H., 2005. Application of a New Grain-Based Reconstruction Algorithm to Microtomography Images for Quantitative Characterization and Flow Modeling. SPE Annu. Tech. Conf. Exhib. 298. https://doi.org/10.2118/95887-MS

Torquato, S., Lu, B., 1993. Chord-length distribution function for two-phase random media. Phys. Rev. E 47, 2950–2953. https://doi.org/10.1103/PhysRevE.47.2950

Tranter, T.G., Kok, M.D.R., Lam., Gostick, J.T., 2018. pytrax: a simple and efficient random walk implementation for calculating the tortuosity tensor of images. https://github.com/PMEAL/pytrax.

van der Walt, S., Schönberger, J.L., Nunez-Iglesias, J., Boulogne, F., Warner, J.D., Yager, N., Gouillart, E., Yu, T., the scikit-image contributors, 2014. scikit-image: image processing in {P}ython. PeerJ 2, e453. https://doi.org/10.7717/peerj.453

Velev, O.D., Lenhoff, A.M., 2000. Colloidal crystals as templates for porous materials. Curr. Opin. Colloid Interface Sci. 5, 56–63. https://doi.org/10.1016/S1359-0294(00)00039-X

Vogel, H.J., Roth, K., 2001. Quantitative morphology and network representation of soil pore structure. Adv. Water Resour. 24, 233–242. https://doi.org/10.1016/S0309-1708(00)00055-5

Wildenschild, D., Sheppard, A.P., 2013. X-ray imaging and analysis techniques for quantifying pore-scale structure and processes in subsurface porous medium systems. Adv. Water Resour. 51, 217–246. https://doi.org/10.1016/j.advwatres.2012.07.018

Zhang, C., Wang, J., Olah, A., Baer, E., 2017. Composite nanofibrous microfiltration water filter. J. Appl. Polym. Sci. 134, 1–12. https://doi.org/10.1002/app.45557

7 Figures and Tables

Feed Inlet

Intra Particle Heat Conduction

Void Convective Heat and Mass transport

Catalyst Bed

Reaction at Void-Solid Interface

Diffusion from void to catalyst particle

Product Outlet
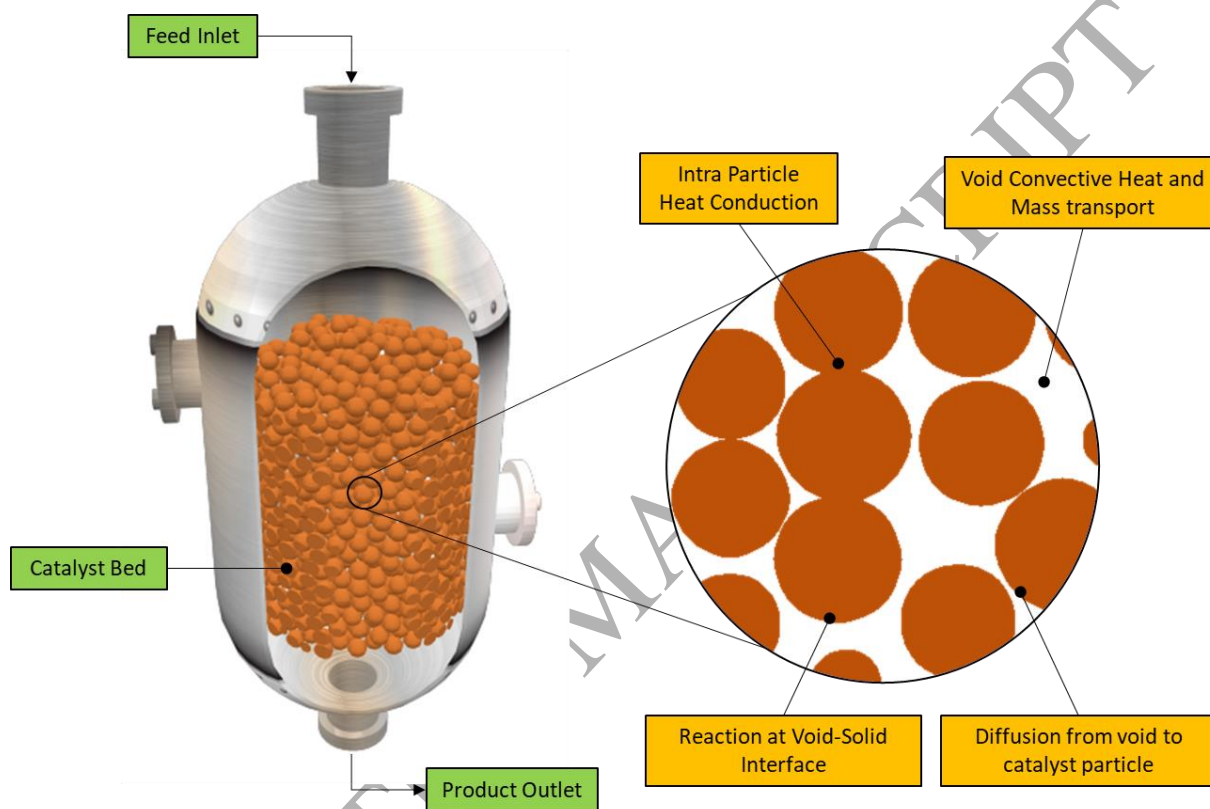
Figure 1 Importance of transport phenomena and reaction processes in solid and void phases of catalytic fixed bed reactor
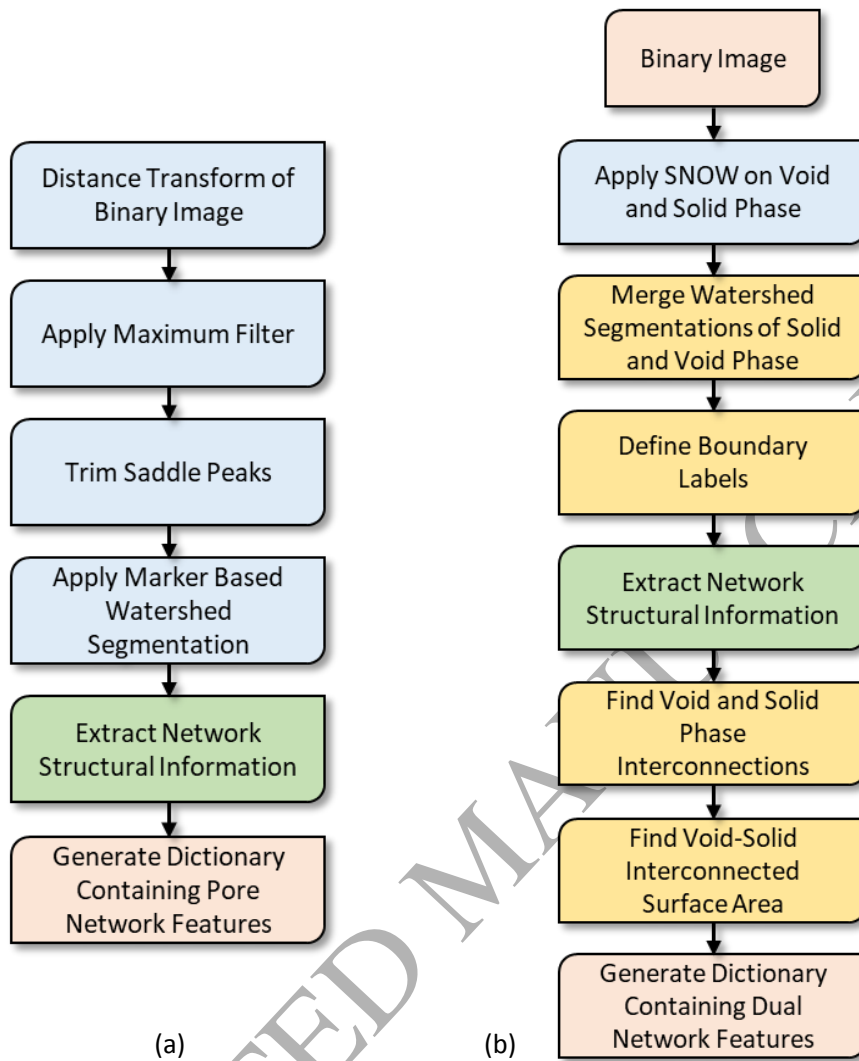
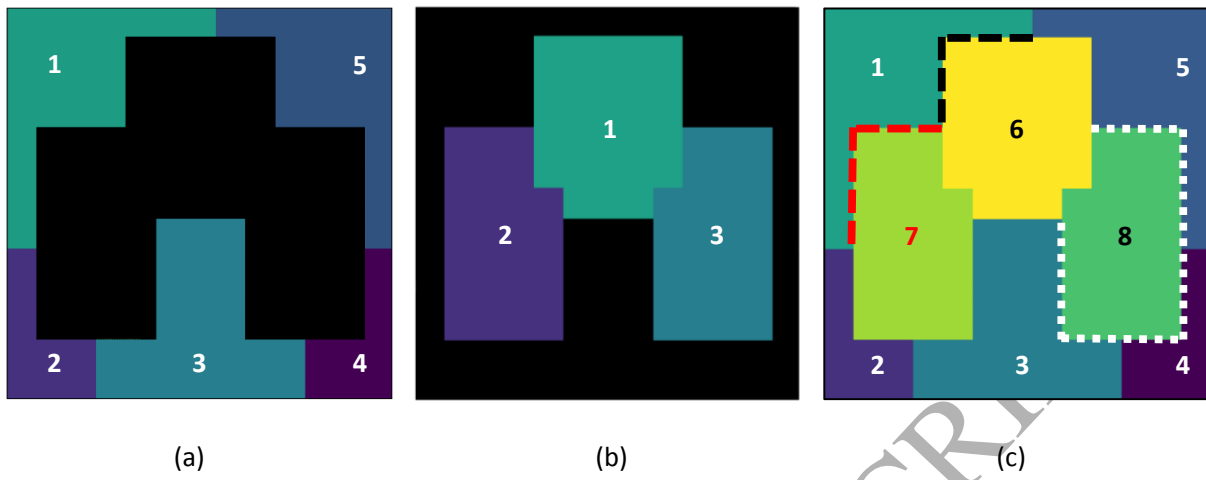Figure 2 a) Void network extraction algorithm using subnetwork of over segmented watershed (SNOW) algorithm b) Dual network extraction algorithm

Figure 3 a) Void phase labeled watershed segmentation, b) Solid phase labeled watershed segmentation c) Merged watershed segmentation of pore and solid regions

(a)   (b)
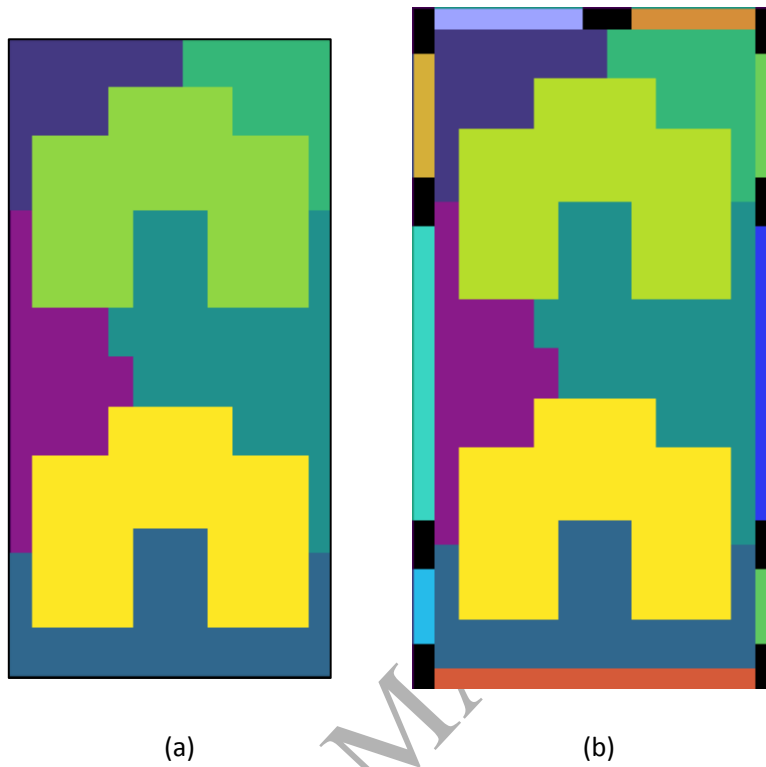
Figure 4 a) Image segmentation without boundary nodes, b) Image segmentation with boundary nodes showing dead zones in black color to avoid boundary nodes interconnections
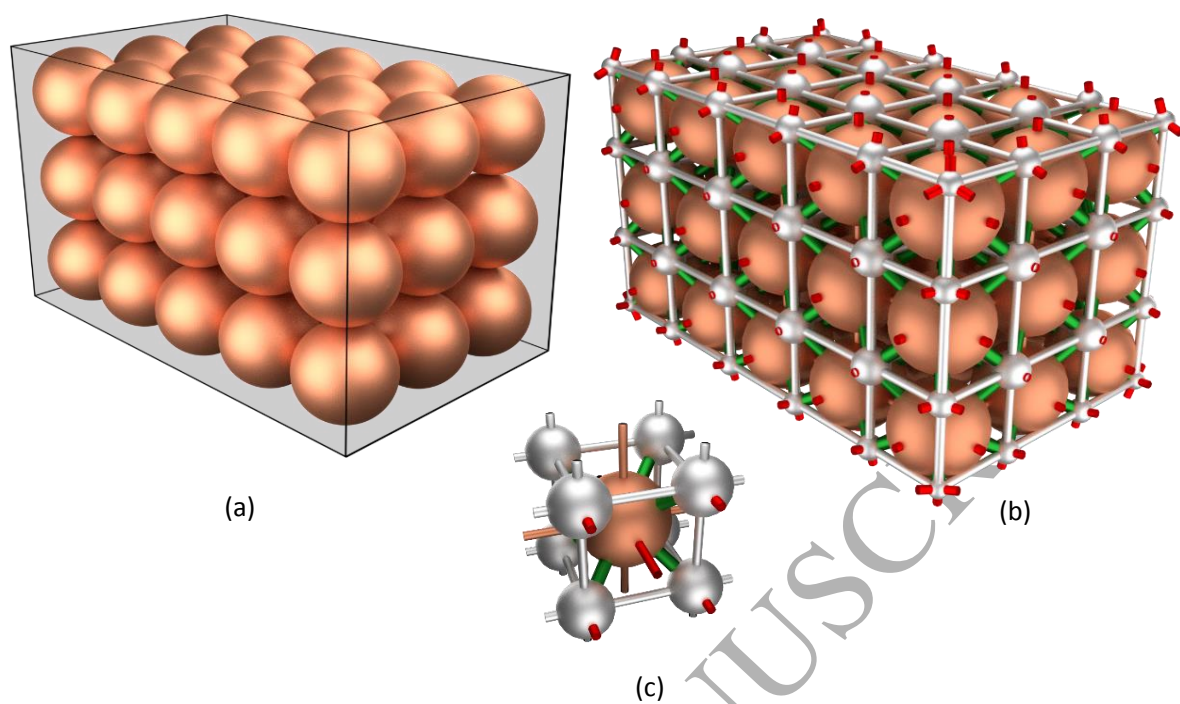
Figure 5 a) Simple cub packing of 45 spheres in a (148,148,249) voxels container, b) Extracted dual network of cubic packing with void and solid phase reprsented in silver and copper color respectively while interconnection and bounda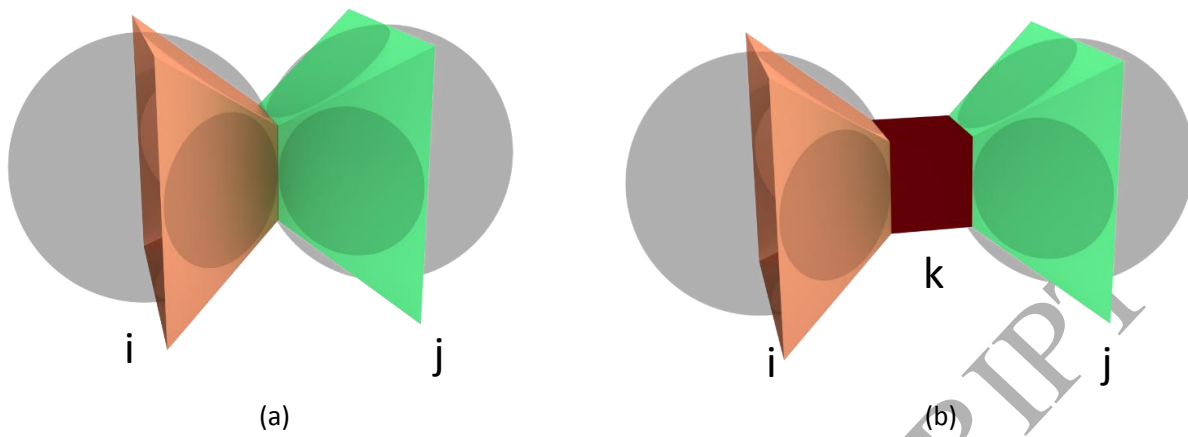ry nodes are represented in green and red color respectively, c) Unit cell of extract dual network for better illustration

| ∅ = 50 mm | ∅ = 54 mm | ∅ = 60 mm | ∅ = 68 mm |
| ε = 44.2% | ε = 31.5% | ε = 16.2% | ε = 5.1% |
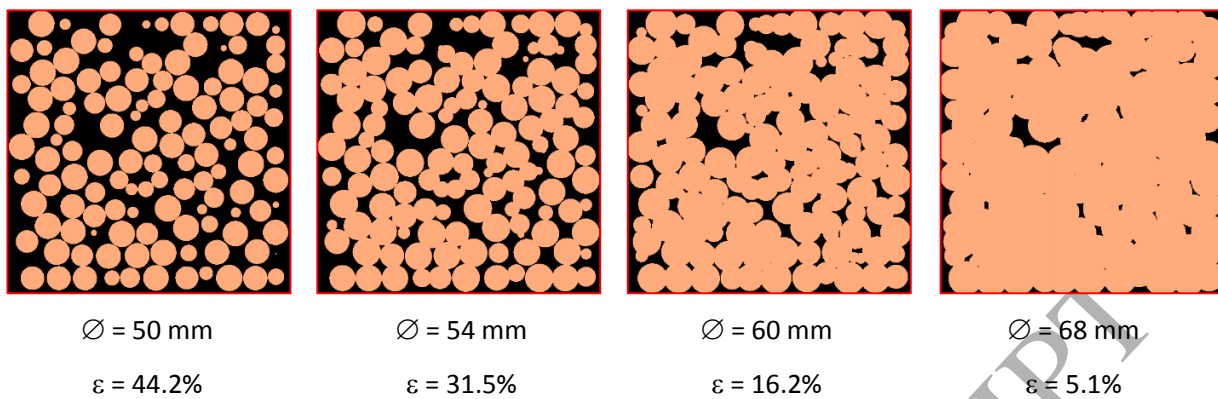
Figure 6 Random sphere packing densification by increasing particle radius from 50 mm to 68 mm

a)   b)   c)
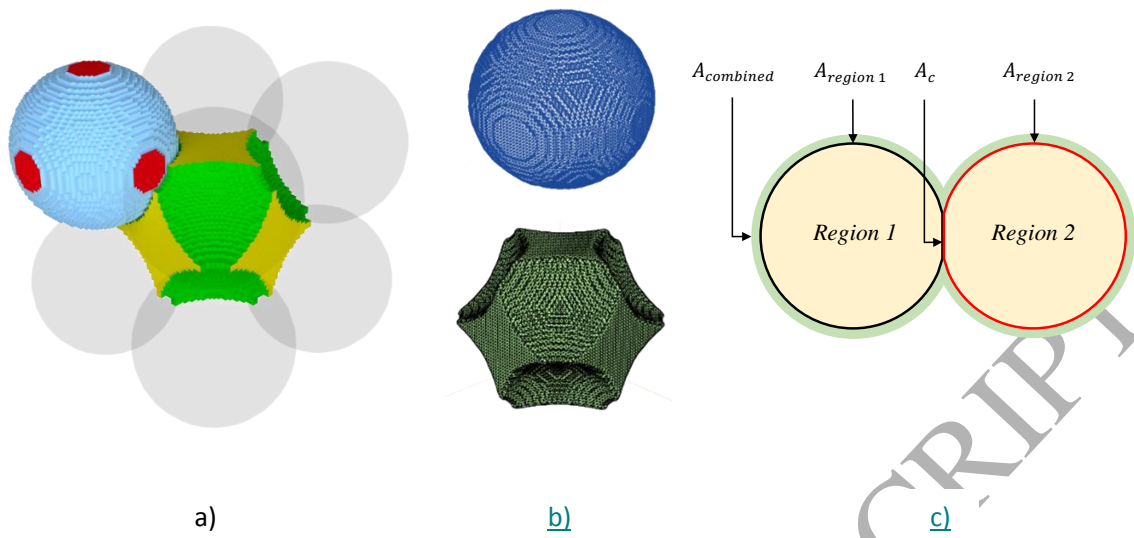
Figure 7a) Interfacial surface area of one solid grain and void in regular cubic packing. Interphase and intraphase interfacial area are shown in cyan and red color for solid and green and yellow color in void respectively. b) Vertex diagram of same solid and void after applying marching cube algorithm in SNOW DUAL. c) Intraphase and interphase surface area calculation schematic using marching cube algorithm

(a)

(b)
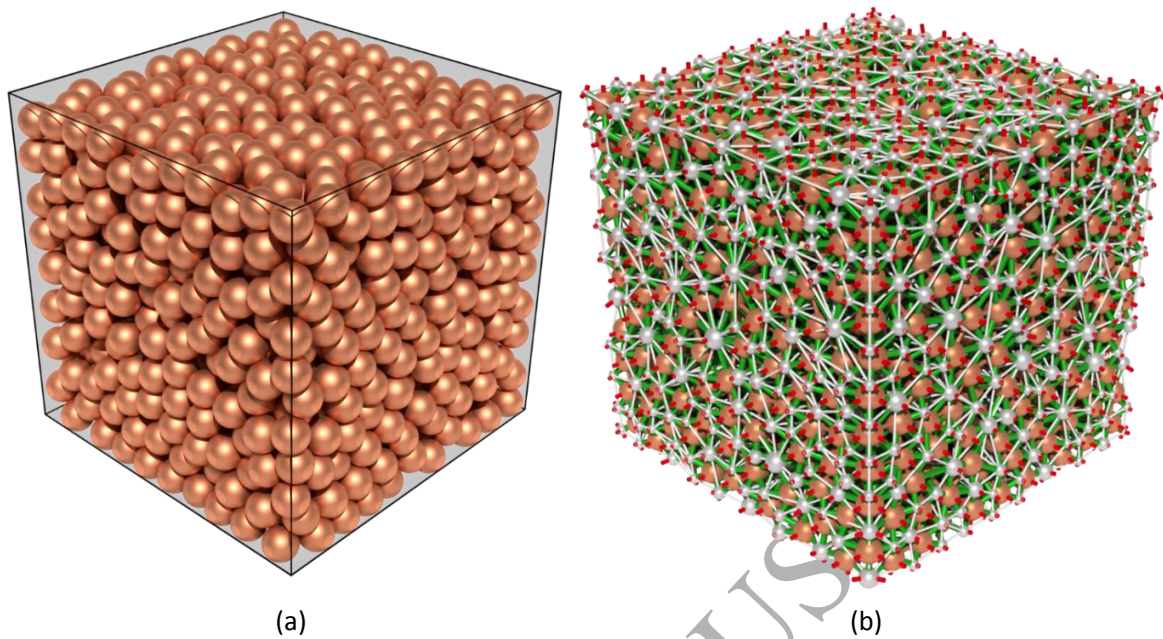
Figure 8 a) Random sphere packing of 1250 spherical particles of 50 voxels diameter in a 525^3 voxel container, b) Extracted dual network of random sphere packing with void and solid phase reprsented in silver and copper color respectvely while interconnection and boundary nodes are represented in green and red color respectvely

Figure 9 a) Square Pyramid model without throats for overlapping spherical particles (Case 1), b) Square pyramid model with throats for void phase of random sphere packing (Case 2)
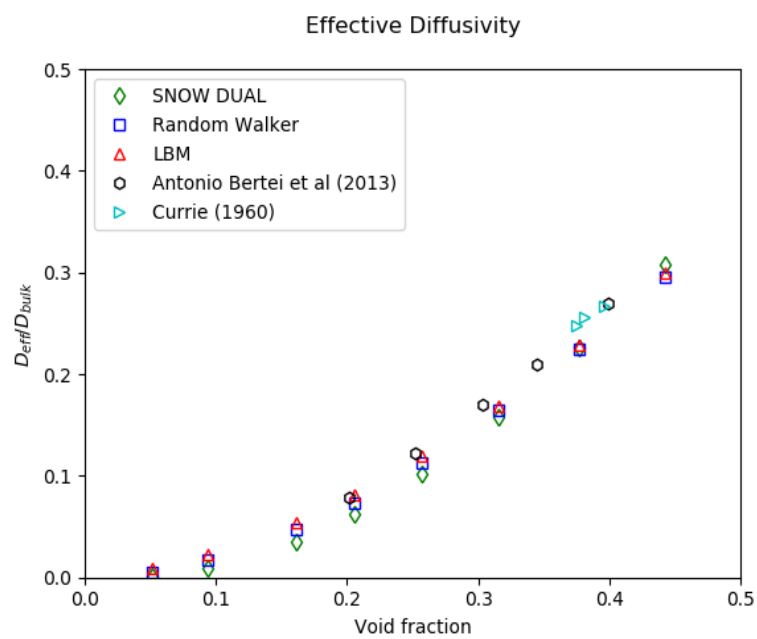
(a)   (b)
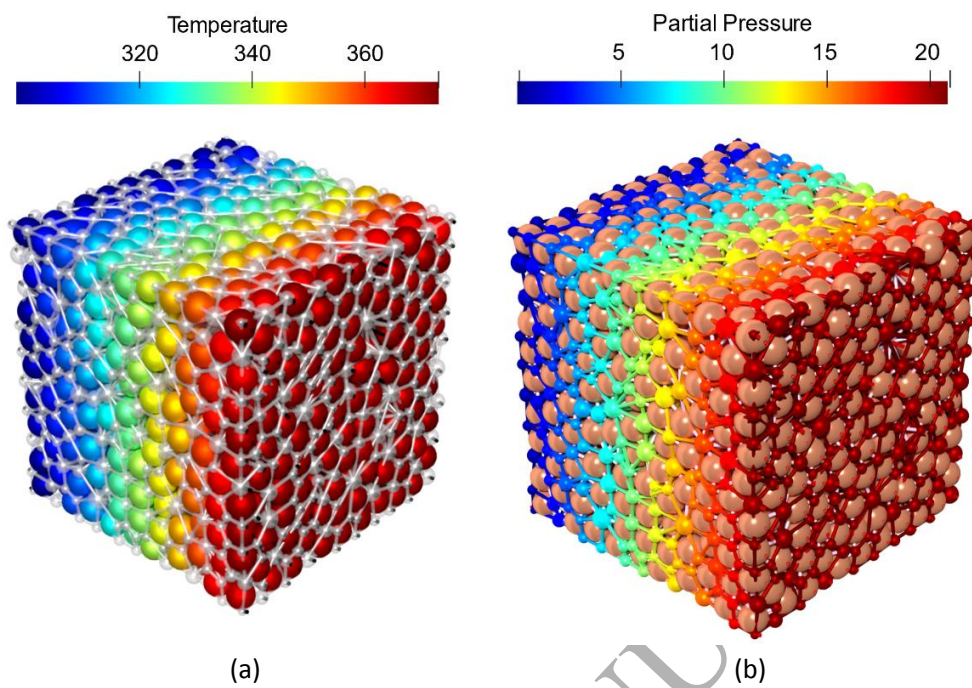
Figure 10 a) 1-dimensional steady state thermal conduction in solid phase, b) 1-dimensional steady state diffusion void phase

Effective Thermal Conductivity

(a)

Effective Diffusivity
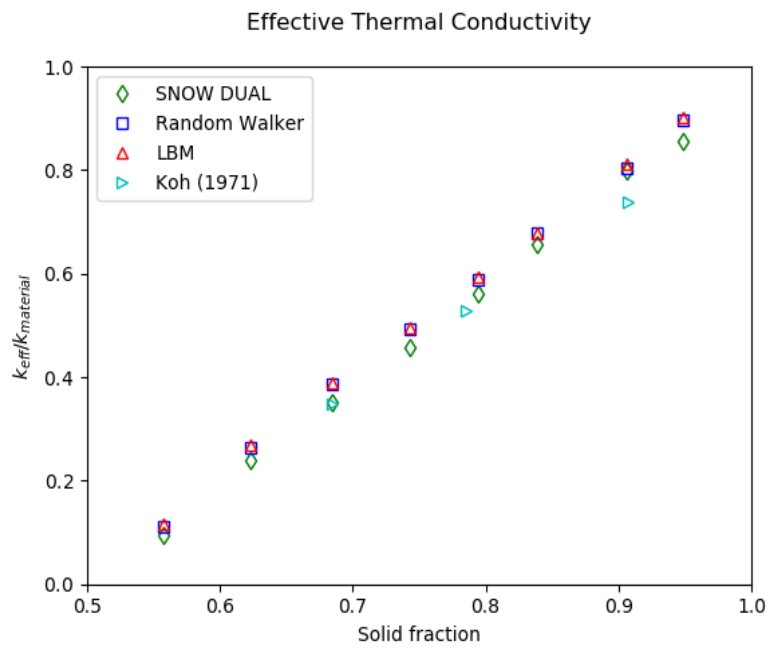
(b)

Figure 11 a) Normalized thermal conductivity in solid phase, b) Normalized diffusivity in void phase of random sphere packing at different porosities
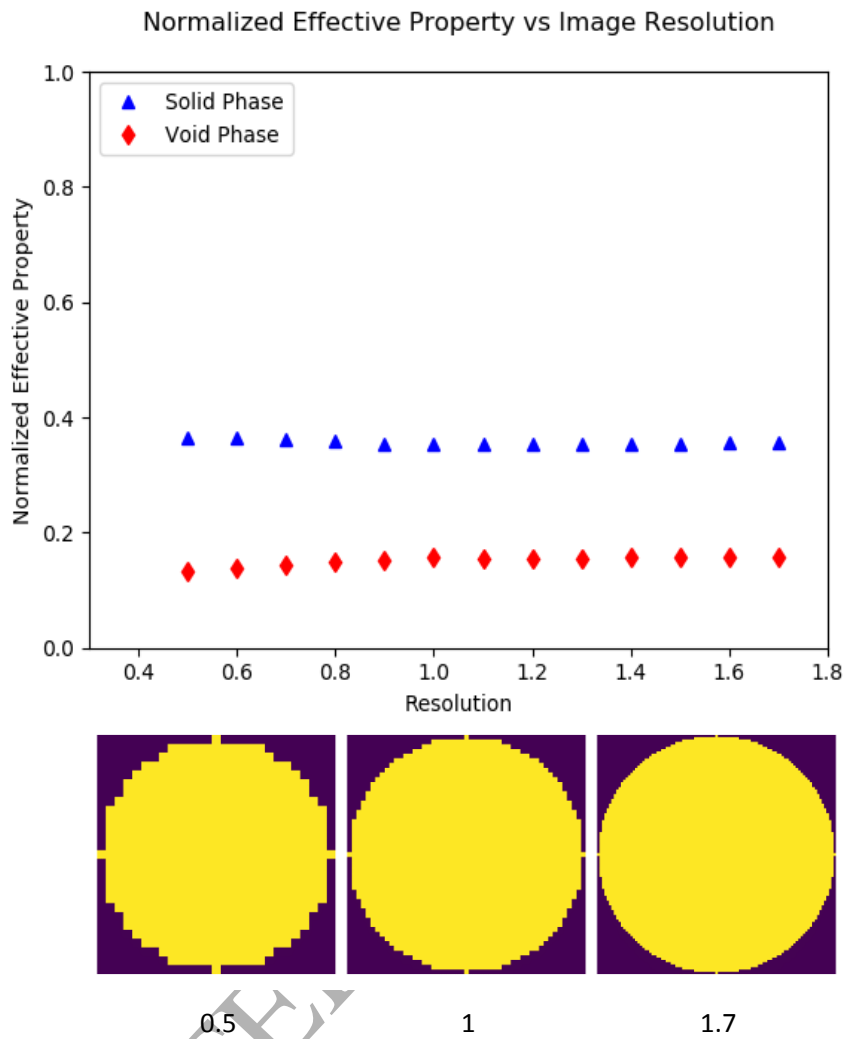
Figure 12 Resolution study of random sphere packing in both void and solid phase.
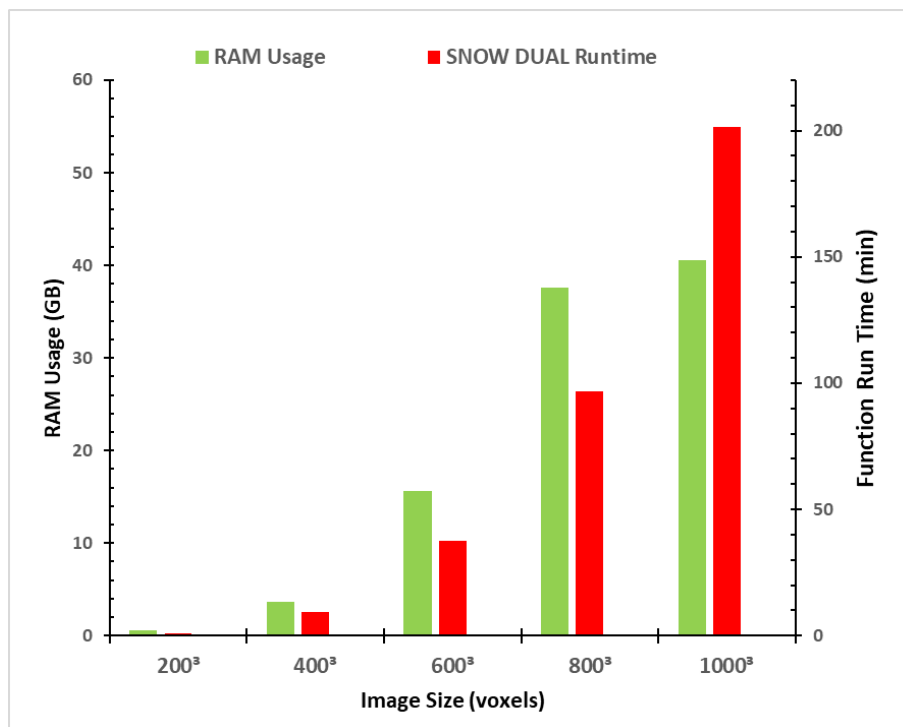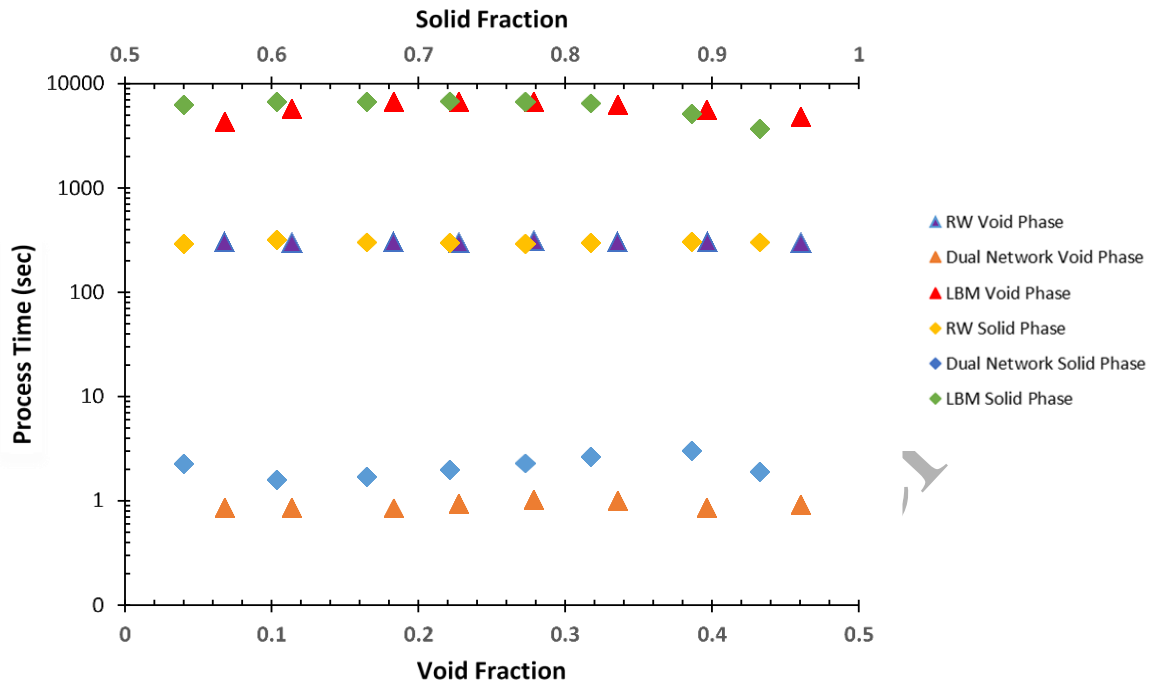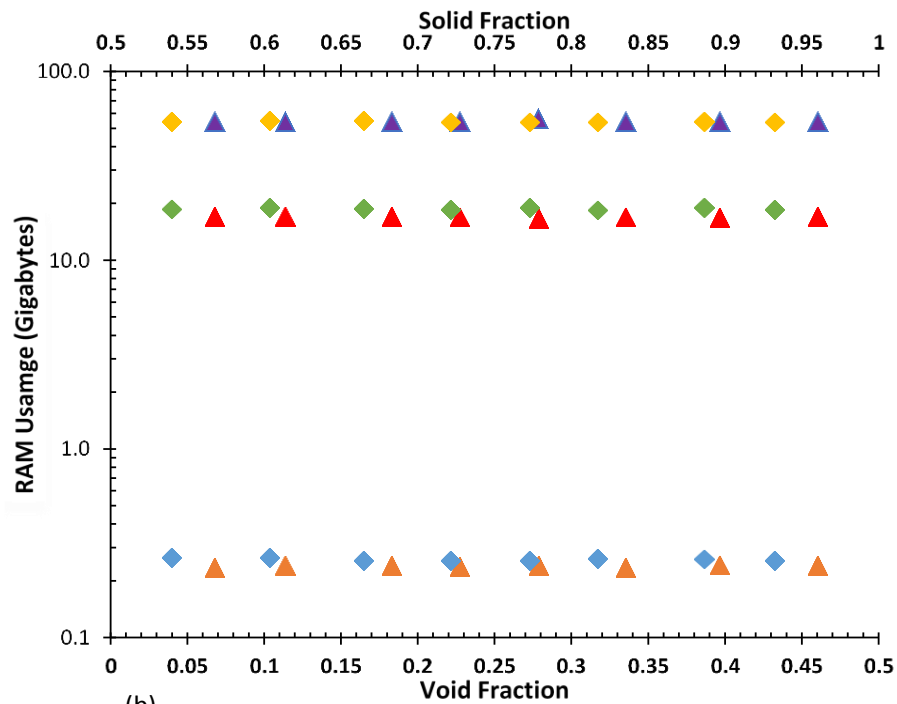
Figure 13 Algorithm run time and memory usage for different image sizes. Simulation were performed on a Dell Precision T5610 Workstation with a Xeon E5-2665 Processor (16 cores) and 128GB of RAM.

Figure 14 a) CPU processing time comparison b) RAM usage comparison in RW, Dual Network and LBM in void and solid phase of random sphere packing

Table 1 Comparison between extracted and theoretically calculated properties of simple cubic packings

Value	Extracted				Theoretical			
Porosity (%)	46.9				46.9			
Solids - N_s	45				45			
Voids - N_v	96				96			
Solids throats - N_{ts}	96				96			
Void throats - N_{tv}	224				224			
Soid-Void Interconnections -N_{int}	360				360			
Boundary Nodes - N_b	206				206			
Coordination Number (Solid Phase)	14				14			
Spheres Diameter (voxels)	49.6				50			
Spheres throat diameter (voxels)	8				8			
	B	F	E	C	B	F	E	C
Coordination Number (Void Phase)	14	10	8	7	14	10	8	7
Voids Diameter (voxels)	48	38	29	23	49	-	-	-
Voids throat diameter (voxels)	23	16	10	10	22	-	9.8	9.26

B,F,E,C are abbrevation of Body, Faces, Edges and Corner respectively

Table 2 Comparison of SNOW DUAL and analytical values of interfacial area in void and solid phase

Phase	SNOW DUAL Interfacial Area	Analytical Solution Interfacial Area	Relative Error (%)
Void Structure:			
Interphase	7396.0	7171	3.04
Intraphase	2760	2937	3.29
Total	10156	10108	0.47
Solid Grain:			
Interphase	7806.17	7851	0.57
Intraphase	3.0	3.0	0
Total	7809.17	7854	0.57